Bioactive Materials 6 (2021) 2729–2741

Contents lists available at ScienceDirect

Bioactive Materials

journal homepage: www.sciencedirect.com/journal/bioactive-materials

Enhanced osteogenesis of titanium with nano-$Mg(OH)_2$ film and a mechanism study via whole genome expression analysis

Mengyu Yao [a,b,1], Shi Cheng [b,1], Guoqing Zhong [b,c], Jielong Zhou [b], Hongwei Shao [a,b], Limin Ma [b], Chang Du [a,*], Feng Peng [b,**], Yu Zhang [b,***]

[a] Department of Biomedical Engineering, School of Materials Science and Engineering, South China University of Technology, Guangzhou, 510641, China
[b] Department of Orthopedics, Guangdong Provincial People's Hospital, Guangdong Academy of Medical Sciences, Guangzhou, Guangdong, 510080, China
[c] Shantou University Medical College, Shantou, 515041, Guangdong, China

ARTICLE INFO

Keywords:
Titanium
Surface modification
Osteogenesis
Whole genome analysis

ABSTRACT

Titanium (Ti) has been the most widely used orthopedic implant in the past decades. However, their inert surface often leads to insufficient osteointegration of Ti implant. To solve this issue, two bioactive $Mg(OH)_2$ films were developed on Ti surfaces using hydrothermal treatment (Ti-M1# and Ti-M2#). The $Mg(OH)_2$ films showed nanoflake structures: sheets on Ti-M1# with a thickness of 14.7 ± 0.7 nm and a length of 131.5 ± 2.9 nm, and on Ti-M2# with a thickness of 13.4 ± 2.2 nm and a length of 56.9 ± 5.6 nm. Both films worked as Mg ions releasing platforms. With the gradual degradation of $Mg(OH)_2$ films, weakly alkaline microenvironments will be established surrounding the modified implants. Benefiting from the sustained release of Mg ions, nanostructures, and weakly alkaline microenvironments, the as-prepared nano-$Mg(OH)_2$ coated Ti showed better *in vitro* and *in vivo* osteogenesis. Notably, Ti-M2# showed better osteogenesis than Ti-M1#, which can be ascribed to its smaller nanostructure. Moreover, whole genome expression analysis was applied to study the osteogenic mechanism of nano-$Mg(OH)_2$ films. For both coated samples, most of the genes related to ECM-receptor interaction, focal adhesion, and TGF-β pathways were upregulated, indicating that these signaling pathways were activated, leading to better osteogenesis. Furthermore, cells cultured on Ti-M2# showed markedly upregulated BMP-4 gene expression, suggesting that the nanostructure with Mg ion release ability can better activate BMP-4 related signaling pathways, resulting in better osteogenesis. Nano-$Mg(OH)_2$ films demonstrated a superior osteogenesis and are promising surface modification strategy for orthopedic applications.

1. Introduction

Currently, for millions of patients who benefit from orthopedic surgery, titanium (Ti) is one of the most frequently used orthopedic implants [1–3]. Despite improvements in surgical procedures, postoperative care, and many other perspectives which all aim to speed up healing after bone implantation, insufficient osteointegration followed by aseptic loosening remains the key limiting factor of biomaterials made of Ti [4–6]. This is because the inert surface of Ti is hard for the newly formed bone to bind. Hence, a bioactive surface of Ti implant is essential for the superior osteointegration, leading to a reduce of aseptic loosening risk.

Surface properties, including physical morphology, released bioactive metal ions, and pH value, are all important parameters for implants to regulate behaviors of osteogenesis-related cells [7–9]. It is widely accepted that micro-roughness surface is beneficial for osteointegration between implant and new bone, because micro-roughness surface has a larger surface area [10]. Surface modification technologies, such as acid etching and sandblasting, are widely used in Ti-based orthopedic implants for clinical applications [11]. Compared with the micro-surface, the nano-surface has a greater influence on bone-related cell behaviors. Nanostructures are more favorable for identification and deposition

---

Peer review under responsibility of KeAi Communications Co., Ltd.

[*] Corresponding author.

[**] Corresponding author.

[***] Corresponding author.

E-mail addresses: duchang@scut.edu.cn (C. Du), peng_feng7@163.com (F. Peng), luck_2001@126.com (Y. Zhang).

[1] The authors contributed equally to this work.

https://doi.org/10.1016/j.bioactmat.2021.02.003
Received 16 December 2020; Received in revised form 1 February 2021; Accepted 2 February 2021

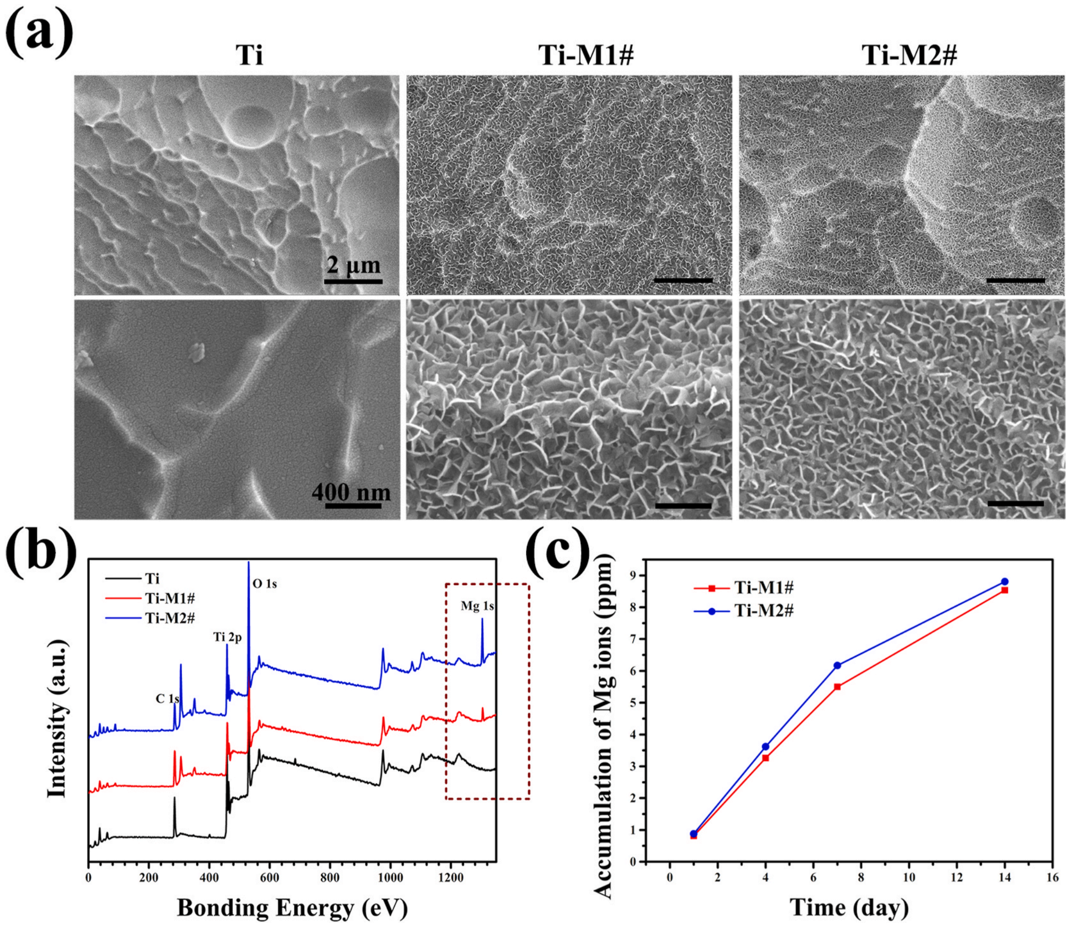

Fig. 1. Surface morphology (a) and full XPS spectrum of Ti, Ti-M1#, and Ti-M2# samples. Cumulative release of Mg ions from Ti-M1# and Ti-M2# samples (c).

Table 1
Elemental compositions of Ti-M1# and Ti-M2# samples.

	Ti (at. %)	O (at. %)	Mg (at. %)
Ti-M1#	39.9	53.5	6.6
Ti-M2#	27.7	58	14.3

of proteins, and can promote adhesion and spreading of cells via interactions with integrin [12]. Incorporating bioactive metal ions into Ti surface is another strategy to enhance osteogenesis behavior of Ti implants. For example, Mg and Ca ions are not only essential elements to maintain bone strength and density, but also improve bone formation and regeneration, while Sr ions can improve bone metabolism and prevent bone loss [13–15]. The pH value, determined by the H^+ and OH^- ions surrounding the implants, can also be used to guide cell fate. Harada et al. found that the optimum pH for alkaline phosphate (ALP) activity was pH 8.5 [16]. Tan et al. fabricated a calcined layered double hydroxide film on Ti to create a local alkaline microenvironment, and found that the ALP activity of rBMSCs was enhanced when cultured on this film [17]. Moreover, an alkaline microenvironment is good for the deposition of hydroxyapatite, which is the main organic component of bone tissue [18–20]. It should be noted that an excessive alkaline microenvironment might be a disadvantage for the proliferation of cells [17]. Though single parameter (bioactive ions/nano-structure/alkaline microenvironment) has all been proved to be benefit for osteogeneses process, but few studies tried to fabricate a surface with all the three characterizations to enhance osteogenic behaviors. Hence, design and construct a multi-characterizations film on Ti with nanostructure, bioactive metal ions release ability, and weakly alkaline microenvironment formation ability remains a challenge and is of great importance for Ti-based orthopedic implants.

On the other hand, the underlying mechanisms of cell behaviors, especially osteogenic behaviors, stimulated by modified surface of Ti remain poorly understood. Several studies have demonstrated the differential expression of RNAs or proteins in specific signaling pathways were related their involvement in cell behaviors [21–23]. For example, Wang et al. found that the expression of p-FAK, p-ERK, p-P38, and p-JNK proteins in rBSMCs were upregulated when cultured on polydopamine-coated polyetheretherketone (PEEK), and concluded that polydopamine could enhance the osteogenic differentiation of rBMSCs through FAK and p38 signaling pathways [23]. However, identify all signaling pathways that may play a crucial role in the osteogenic differentiation of stem cells remains a challenge. In recent years, whole genome expression analysis technology has been rapidly developing. By detecting the RNA expression of all the genes, researchers can conduct a comprehensive evaluation of all the signaling pathways related to cell behaviors, and thus obtain information regarding the molecular mechanisms underlying various cell behaviors stimulated by biomaterials [24–26]. Hence, using whole genome expression technology can fully and comprehensively understand the underlying molecular mechanism between cells and biomaterials, and then offer guidance for the design of biomaterials.

In the present study, to construct nanostructured film with the ability to release bioactive ions and create a weakly alkaline microenvironment, we used hydrothermal treatment to fabricate nanostructured $Mg(OH)_2$ films on Ti surface. The decomposition of $Mg(OH)_2$ films would not only result in the release of Mg ions, but also result in the release of OH^-, thus forming a weakly alkaline microenvironment surrounding the implant. The osteogenesis potential of the resulting nano-$Mg(OH)_2$-

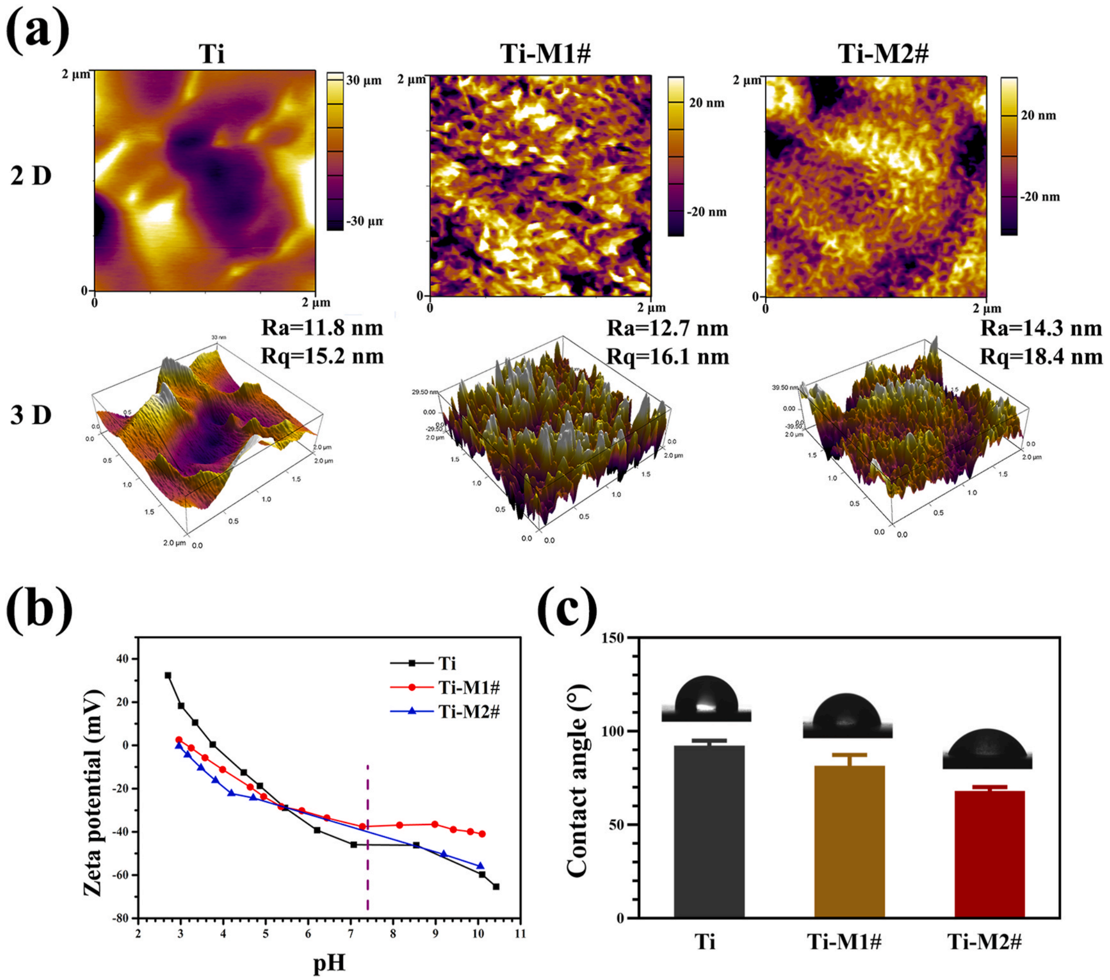

Fig. 2. Two-dimensional (2D) and three-dimensional (3D) topography of Ti, Ti-M1#, and Ti-M2# samples (a). Surface zeta potential (b) and water contact angle (c) of Ti-M1# and Ti-M2# samples.

coated Ti was evaluated using *in vitro* culturing murine C3H10T1/2 cells and an *in vivo* bone defect model. The molecular mechanism of enhanced osteogenesis of the nano-$Mg(OH)_2$ film was explored using whole genome expression analysis.

2. Materials and methods

2.1. Sample preparation and characterization

Commercial pure Ti (purity > 99.85%) was cut into 10 × 10 × 1 mm and 20 × 20 × 1 for *in vitro* experiments, and 10 × Φ 2 mm for *in vivo* experiments. The specimens were treated with HF and HNO_3 mixed aqueous solution to remove the oxide layer. For hydrothermal treatment, the cleaned Ti was placed in a Teflon-lined stainless steel, and then gently added to 50 mL of a solution containing 1.2 mM $MgCl_2$ and 21.6 mM urea. Immediately, the stainless steel was programmed to reach 120 °C and kept for 12 h. The obtained samples were cleaned with deionized water and denoted as Ti-M1#. Furthermore, Ti samples hydrothermally treated in solution containing 6 mM $MgCl_2$ and 108 mM urea were denoted as Ti-M2#.

A field-emission scanning electron microscope (FE-SEM; Merlin; Carl Zeiss AG, Germany) was used to observe the surface morphology. Surface roughness was examined using an atomic force microscope device (AFM; MFP-3D-S; Asylum Research, USA) in tapping mode. The mean roughness value (Ra) represents the arithmetic average of the deviation from the center plane of the sample and Rq represents the root-mean-square deviation of the surface. X-ray photoelectron spectroscopy (XPS; EscaLab Xi+; Thermo Fisher Scientific, USA) was used to analyze the surface chemical compositions.

2.2. Ion release

The samples were immersed in 10 mL of deionized water at 37 °C for 1, 4, 7 and 14 days. The extract solutions of various samples were collected at each time point. The amount of released Mg ions was quantified via inductively coupled plasma atomic emission spectroscopy (ICP-MS; iCAP RQ; Thermo Fisher Scientific, USA).

2.3. Water contact angle

The water contact angle was determined through goniometry using a static water drop method. Contact angles were measured with distilled water using the contact angle measuring system (OCA15; Dataphysics, Germany). A drop of water with a volume of 4 ± 0.2 μL was deposited on the surface.

2.4. Surface zeta potentials

A surpass electrokinetic analyzer (Anton Parr, Austria) was used to detect the surface zeta potential. Briefly, two samples (20 × 10 × 1 mm) were fixed face to face on the holder with a gap of 100 ± 5 μm. The electrolyte solution was KCl solution (1 mM), and its pH was adjusted using HCl and NaOH (0.05 M). The surface zeta potential was calculated according to the Helmholz-Smoluchowski equation:

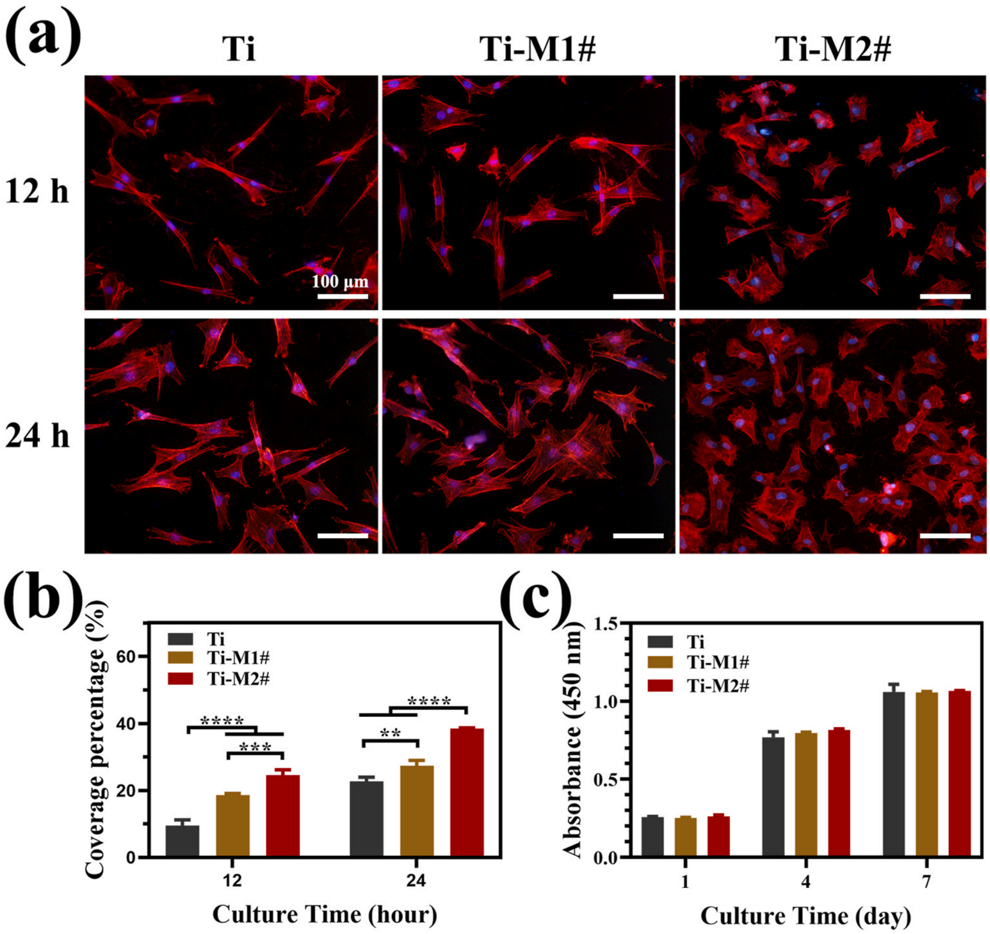

Fig. 3. Fluoroscopy images of murine C3H10T1/2 cells stained with anti-vinculin and DAPI cultured on various samples for 12 and 24 h (a) and calculated coverage percentage (b). Cell proliferation of murine C3H10T1/2 cells cultured on various samples for 1, 4 and 7 days (c).

$$\zeta = \frac{dU}{dP} \times \frac{\eta}{\varepsilon \times \varepsilon 0} \times C \tag{1}$$

where ζ denotes the zeta potentials, dU/dP is the slope of the streaming potential and pressure, and η, ε, ε_0, and C represent the electrolyte viscosity, dielectric constant, vacuum permittivity, and conductivity, respectively.

2.5. Cell experiments

2.5.1. Cell culture

Murine C3H10T1/2 cells (ZQ 0452, Shanghai Zhong Qiao Xin Zhou Biotechnology Co., Ltd. China), which are isolated from the embryo of C3H mice, were used to evaluate the *in vitro* performance of various samples. The cells were cultured in MEM (ZQ-300, Shanghai Zhong Qiao Xin Zhou Biotechnology Co.,Ltd. China) supplemented with 1% Glutamax, 1% sodium pyruvate, 10% fetal bovine serum and 1% penicillin-streptomycin at 37 °C in a humidified atmosphere of 5% CO_2. Prior to the test, the samples were sterilized in a high-pressure steam sterilization pot for 20 min.

2.5.2. Cell adhesion and proliferation

The samples (10 × 10 × 1 mm) were placed in 24-well plates and then seeded with cells (2×10^5 cell/mL). After 12 and 24 h of culture, the samples from each group were rinsed with PBS three times, and then fixed in 4% paraformaldehyde for 30 min at 4 °C. The cells were then permeabilized with 0.2% (v/v) Triton-X100 (Sigma) for 10 min. Non-specific binding sites were blocked by incubating the samples in bovine serum albumin for 1 h. Anti-vinculin (400 μl) was added and the cells were cultured for 1 h at 37 °C. Finally, the cells were stained by DAPI away from any light for 30 min. Between each step, the samples were rinsed with PBS. The stained cells were observed using a fluorescence microscope (80i; Nikon, Japan).

The samples (10 × 10 × 1 mm) were placed in 24-well plates and then seeded with cells (2×10^5 cell/mL). Cell proliferation was evaluated on days 1, 4, and 7 using CCK-8 assay. Briefly, 10% CCK-8 solution was added to each sample and incubated at 37 °C for 2 h. Aliquots from each sample (100 μL) were transferred into a 96-well plate and absorbance was measured at a wavelength of 450 nm using a microplate reader (Multiskan Go; Thermo Fisher Scientific, USA).

2.5.3. Extracellular matrix (ECM) mineralization

The samples (10 × 10 × 1 mm) were placed in 24-well plates and then seeded with cells (1×10^5 cell/mL). After 1 day of culture, the original culture medium was replaced with culture medium supplemented with osteogenic induction solution (strain C57BL/6 Mouse Adipose-derived Mesenchymal Stem Cells Osteogenic Differentiation Medium (RASMD-90021); Cyagen Biosciences Inc., China)). After 7 and 14 days of culture, ECM mineralization were quantified by Alizarin red staining. Briefly, the cells were washed three times with PBS, fixed for 1 h in ice-cold 70% ethanol, and rinsed three times with deionized water. The cells were stained for 30 min with 40-mM alizarin red solution at 37 °C, and excess dye was removed gently with PBS. Calcification deposits, which appeared bright red, were identified using a stereoscopic microscope (SMZ25; Nikon, Japan). Quantification was performed as follows. Next, 40 μL of 10% hexadecylpyridine was added to each sample and the aliquots from each sample (100 μL) were transferred into

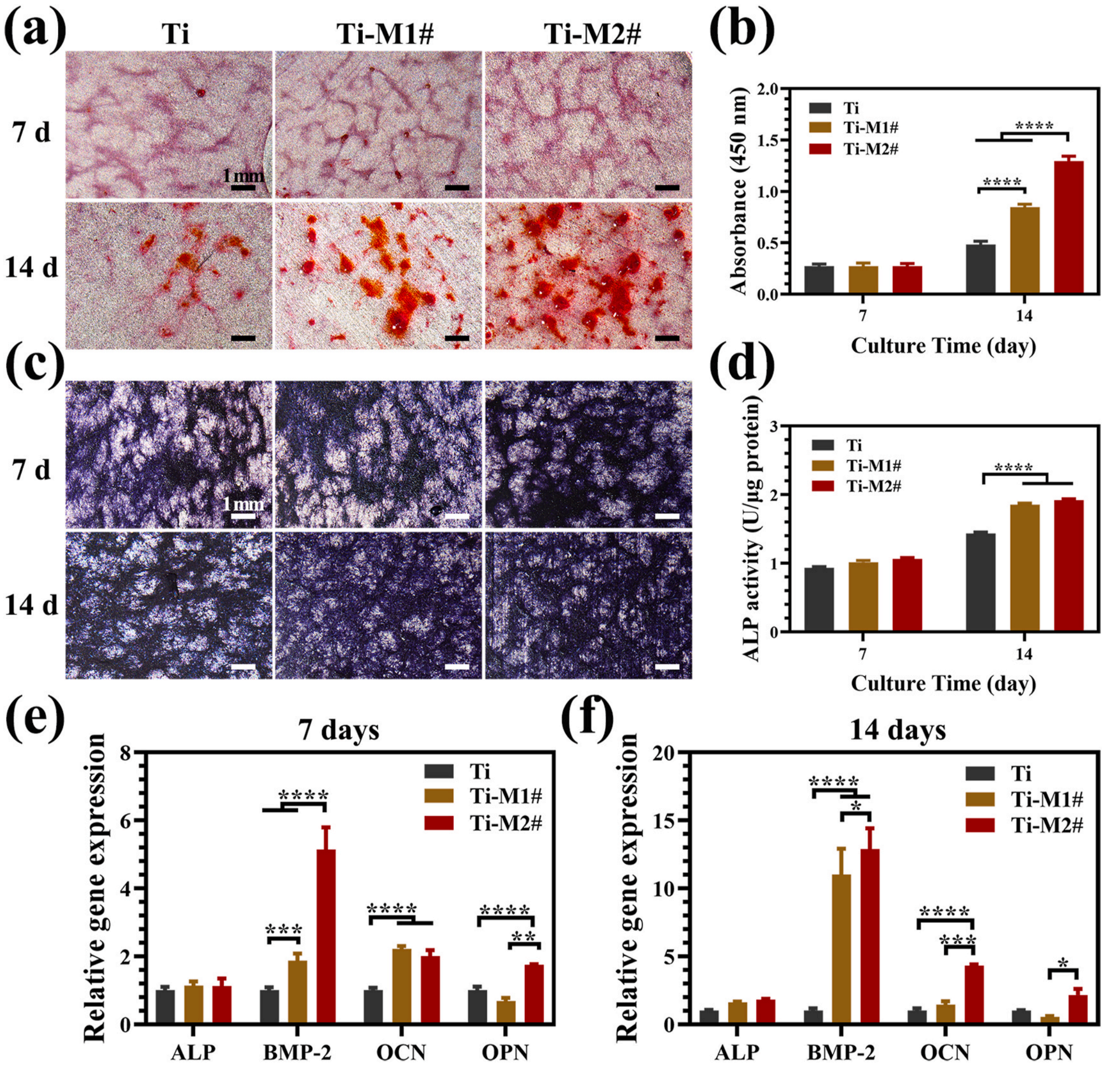

Fig. 4. Alizarin red staining of murine C3H10T1/2 cells cultured on various for 7 and 14 days (a) and corresponding quantitative analysis (b). Images of ALP staining of murine C3H10T1/2 cells cultured on various samples for 7 and 14 days (c) and corresponding quantitative analysis (d). Relative mRNA expression of osteogenesis-related genes of murine C3H10T1/2 cells cultured on various samples for 7 days (e) and 14 days (f). (For interpretation of the references to colour in this figure legend, the reader is referred to the Web version of this article.)

a 96-well plate and for absorbance was measured at a wavelength of 620 nm using a microplate reader.

2.5.4. Alkaline phosphatase (ALP) activity

The cells were cultured as described in the ECM mineralization assessment. The ALP activity of each sample was assessed after 7 and 14 days of culture. The content of ALP was determined using an alkaline phosphatase assay kit (Beyotime, China), and the content of intracellular protein was determined using a BCA protein assay kit (Beyotime, China). The quantitative result of ALP activity was determined by the ratio of ALP content to BCA content. Furthermore, ALP was stained with BCIP/NBT Alkaline Phosphatase Color Development Kit (Beyotime, China), and images were obtained using a stereoscopic microscope.

2.5.5. Quantitative real-time PCR (RT-PCR) analysis

The expression levels of four osteogenesis-related genes, namely bone morphogenetic protein 2 (BMP-2), alkaline phosphatase (ALP), osteocalcin (OCN) and osteopontin (OPN), were evaluated using qRT-PCR. The samples (20 × 20 × 1 mm) were placed in 6-well plates and seeded with cells (2.5 × 10^5 cells/mL). After 1 day of culture, the original culture medium was replaced with culture medium supplemented with osteogenic induction solution. After 7 and 14 days of culture, total RNA was extracted using Trizol (Sigma Aldrich, USA) and then quantified by Nanodrop 2000 (Thermo fisher scientific, USA). Next, 1 μg of RNA was reverse transcribed into cDNA using the 1st Strand cDNA synthesis supermix Kit (Yeasen, China), and then mixed with SYBR Green Mastermix and primers to quantify the gene expression of the target genes. GAPDH was used as a housekeeping gene. The primer sequences are listed in Table S1.

2.6. In vivo study

All animal experiments were approved by the Animal Ethics Committee of Guangdong Provincial People's Hospital and applied in accordance with the Guidelines for Care and Use of Laboratory Animals of Southern Medical University.

2.6.1. Implantation surgery

Thirty-six Sprague-Dawley (SD) rats with ages of 5-week-old were divided into 3 groups ($n = 12$ for per group). The rats were anesthetized with 3% pentobarbital sodium (30 mg/kg dose) by intraperitoneal injection, and then sterilized with 2% iodine at the implanted site. An incision of about 1.5 cm was made at the distal side of the femur. The patella was pushed inward and a hole with a diameter of 2 mm was

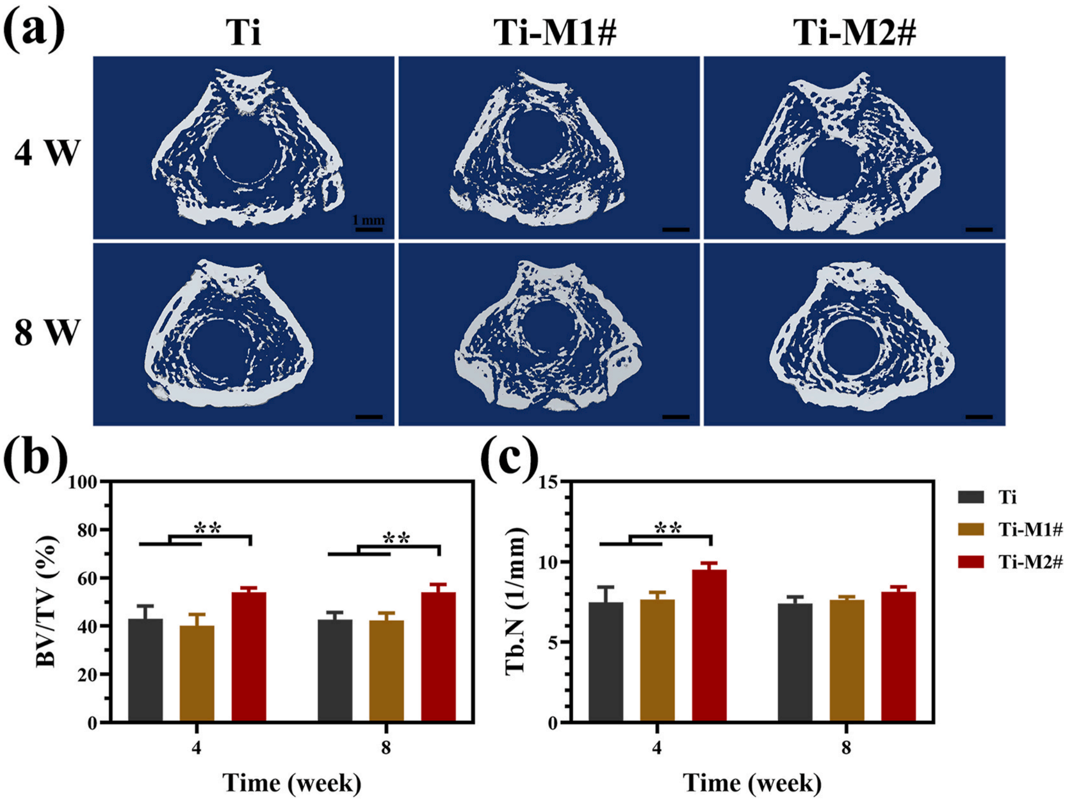

Fig. 5. Representative 3D-reconstructred micro-CT images of the harvested femur (a). Quantitative analysis of micro-CT, including BV/TV (b) and Tb.N (c).

drilled along the major axis of the femur. Then, the corresponding rod-shaped material was implanted. The wound was washed and sterilized with 2% iodine. Each rat was injected with benzylpenicillin sodium (400,000 units/kg) consecutively for 3 days after surgery to avoid infection. The rats were sacrificed by over-injecting chloral hydrate at 4 and 8 weeks after surgery.

2.6.2. *Micro-CT analysis*

The bone samples obtained were scanned using a micro-CT analyzer (Inveon™ Multi-Modality; Siemens Medical Solutions, Inc., Malvern, PA, USA). The scanning thickness was 9.1 μm at 80 kV and 500 μA. The three-dimensional (3D) image of each sample was reconstructed using the Inveon™ Image Research Workplace (Siemens, German). Furthermore, the volume/total volume (BV/TV) and trabecular number (Tb.N) values were analyzed.

2.6.3. *Sequential fluorescent labeling assays*

Sequential fluorochrome labeling was performed by intraperitoneally injecting two fluorochromes into the rats. Briefly, 30 mg/kg Alizarin red and 25 mg/kg tetracycline hydrochloride (Sigma Aldrich, USA) were injected at 4 and 6 weeks post-surgery, respectively. The femurs with implants were fixed in formalin, dehydrated with ethanol, and then embedded in polymethylmethacrylate (PMMA). The embedded specimens were cut, ground, and polished. Fluorochromes labeling of the sections was observed by confocal laser scanning microscopy (CLSM; Olympus). The values of mineral apposition rate (MAR) and bone formation rate/bone surface (BFR/BS) were analyzed using the fluorochromes labeling results.

2.6.4. *Histological evaluation*

After micro-CT scanning, the fixed femur specimens were sliced, as described in section 2.6.3. The sections were stained with methylene blue acid fuchsin solution to visualize the bone-implant interfaces and imaged using a stereoscopic microscope. The bone-implant percentages were determined using these images.

2.6.5. *Push-out force*

The surface muscles and tendon tissues on the obtained femur were removed. Then, the distal bone tissues of the femur were carefully stripped to expose the cylindrical materials about 2 mm from the distal end for mechanical testing. The other end of the femur was fixed in epoxy. The push-out force was detected using a universal material testing machine (Instron 5697, USA) according to the test standard DIN EN ISO 527-1.

2.7. *Whole genome expression analysis*

Whole genome expression analysis was carried out after culturing murine C3H10T1/2 cells on various samples in triplicate for 12 h. Total RNA was isolated and purified using TRIzol reagent (Invitrogen, Carlsbad, CA, USA). Poly (A) RNA was purified from 1 μg of RNA and fragmented into small pieces. The cleaved RNA fragments were then reverse-transcribed to create cDNA using SuperScript™ II Reverse Transcriptase (cat. 1896649; Invitrogen, USA). U-labeled second-stranded DNAs were then synthesized using the obtained DNA and RNA. Finally, 2 × 150 bp paired-end sequencing (PE150) was conducted on an Illumina Novaseq™ 6000 (LC-Bio Technology Co., Ltd., Hangzhou, China) according to the manufacturer's protocol. Cutadapt software was used to remove reads that contained adaptor contamination. HISAT2 software was used to map reads to the genome and then assembled using StringTie. Then, all transcriptomes from all samples were merged to reconstruct a comprehensive transcriptome using gffcompare software. The expression values were selected with fold change >2 or <0.5 and p value < 0.05 using the R package edgeR, and defined as differentially expressed genes (DEGs). The gene ontology (GO) enrichment and Kyoto Encyclopedia of Genes and Genomes (KEGG) databases were analyzed to identify potential pathways.

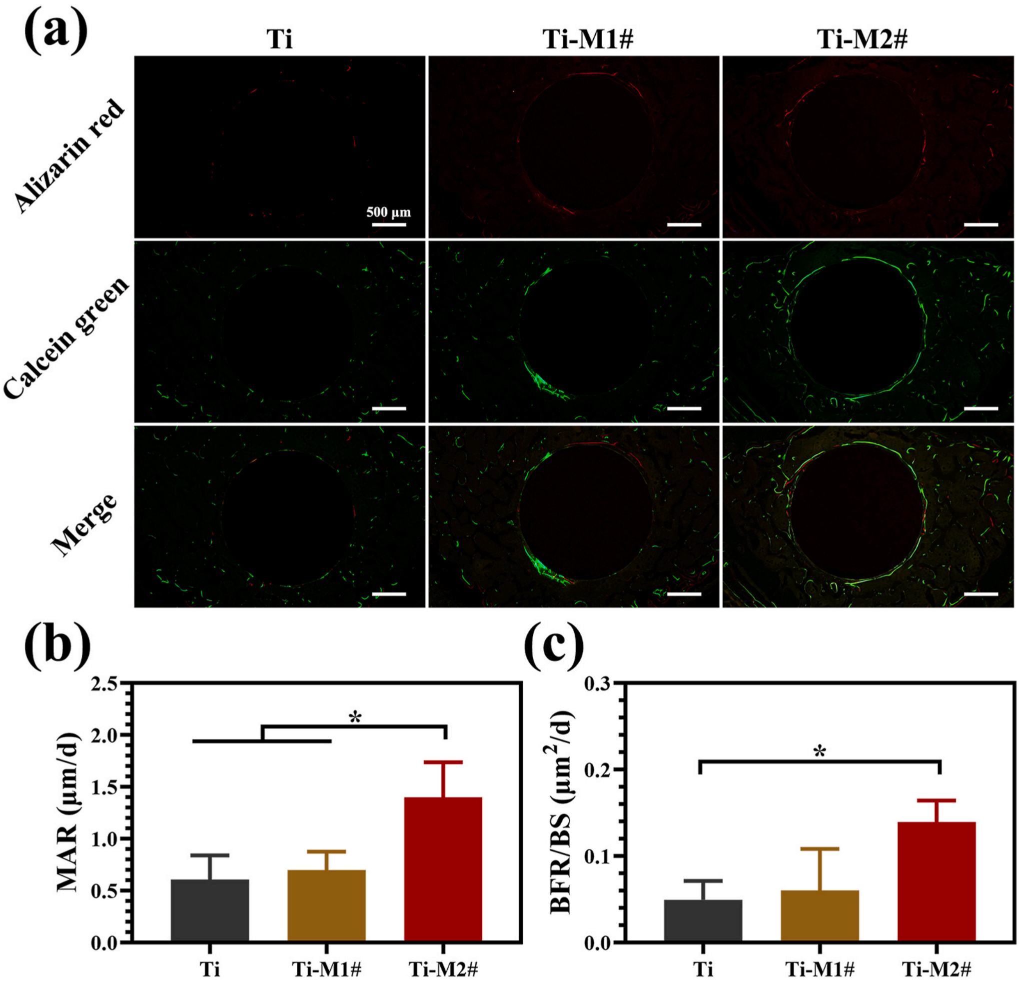

Fig. 6. Sequential fluorescent labeling of new bone formation (a). Quantitative analysis of sequential fluorescent labeling, including MAR (b) and BFR/BS (c).

2.8. *Statistical analysis*

Data were expressed as mean ± standard deviations (SD) and analyzed using GraphPad Instant Software (GraphPad Prism Software, Inc., USA). A two-way analysis of variance (ANOVA) with Tukey-Kramer multiple comparison post-test was applied. $P < 0.05$ was considered to be statistically significant.

3. Results and discussion

3.1. *Surface physicochemical properties of nano-$Mg(OH)_2$ coated Ti*

The surface morphologies of Ti, Ti-M1#, and Ti-M2# samples are shown in Fig. 1a. Mixed acid treated Ti exhibited a typically ridged surface [27]. After hydrothermal treatment, the surfaces were covered by nano-sheet structures (Ti-M1# and Ti-M2#). The thickness and length of the sheets on Ti-M1# surface were 14.7 ± 0.7 nm and 131.5 ± 2.9 nm, respectively, while for the sheets on Ti-M2# surface, the parameters were 13.4 ± 2.2 nm and 56.9 ± 5.6 nm, respectively. These results suggested that the nano-sheets on Ti-M2# sample were significantly smaller than those on Ti-M1# sample. The full XPS spectra of all the samples are displayed in Fig. 1b. A significant Mg 1s peak at 1300 eV was detected for Ti-M1# and Ti-M2# surfaces. The peak intensity of Mg peak of Ti-M2# sample was stronger than that of Ti-M1# sample. Further quantitative analysis indicated that the Mg contents for Ti-M1# and Ti-M2# samples were 6.6 at% and 14.3 at%, respectively (Table 1). Fig. 1c shows the cumulative release of Mg ions from Ti-M1# and Ti-M2# samples. Both samples exhibited a sustained release of Mg ions, while Ti-M2# sample exhibited a slightly higher release rate than Ti-M1# sample, which could be ascribed to the higher content of Mg on the surface of Ti-M2# (Table 1).

In this study, the hydrothermal solution contained urea and Mg^{2+} ions. The urea will hydrolyze to form NH_3 and CO_2 when the temperature reaches up to 60 °C. Therefore, the reaction occurring in the Teflon-lined stainless steel can be described as follows:

$$CO(NH_2)_2 + H_2O \rightarrow 2NH_3 + CO_2 \tag{2}$$

$$NH_3 + H_2O \rightarrow NH_4^+ + OH^- \tag{3}$$

$$Mg^{2+} + 2OH^- \rightarrow Mg(OH)_2 \tag{4}$$

According to the above reactions, it can be concluded that the nano-sheet deposited on Ti-M1# and Ti-M2# were product of $Mg(OH)_2$. The detection of Mg on the coated samples and the release of Mg ions from the coated surface further proved this speculation. Unfortunately, the characteristic peak of $Mg(OH)_2$ was not detected by XRD (Fig. S1a), which might because the thickness of $Mg(OH)_2$ film was too thin to be detected (Fig. S1b). The higher concentration of urea and Mg^{2+} ions of Ti-M2# hydrothermal solution means more crystal nucleus would formed on Ti-M2# surface, resulting in smaller $Mg(OH)_2$ structures. More importantly, the dissolution of $Mg(OH)_2$ film would not only release Mg^{2+} ions, but also produce OH^- ions near the $Mg(OH)_2$ coated surface. Therefore, a nano-$Mg(OH)_2$ coated film on Ti not only can works as a release platform for Mg^{2+} ions, but also results in a weakly alkaline microenvironment.

The surface roughness and topography were evaluated by AFM. The

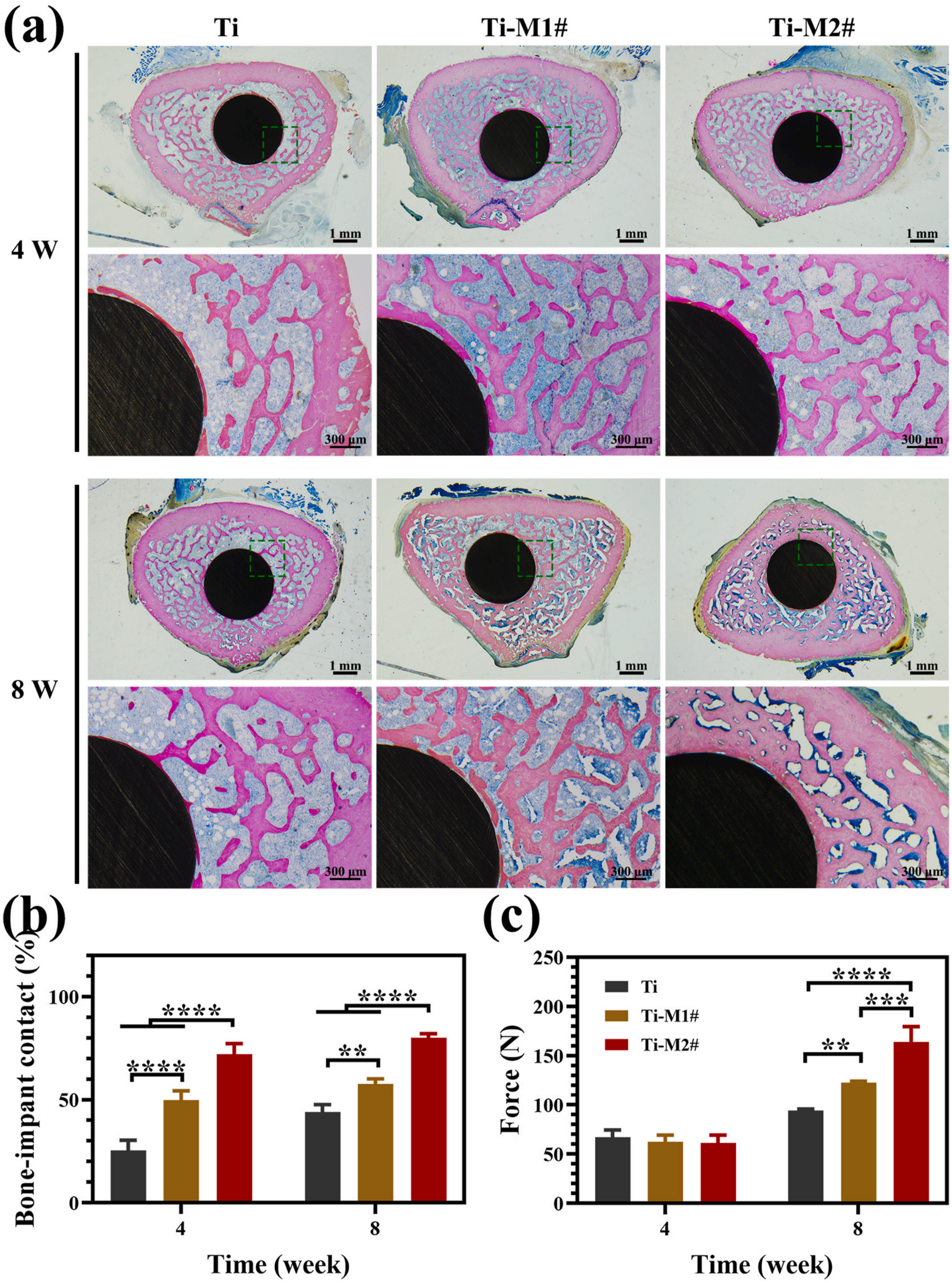

Fig. 7. Histological observation of the tissue sections stained with methylene blue acid fuchsin 4 and 8 weeks after implantation (a). Histogram of the percentages of the bone-implant contact ratios (b). Push-out forces of Ti, Ti-M1#, and Ti-M2# samples implanted in the femur for 4 and 8 weeks (c). (For interpretation of the references to colour in this figure legend, the reader is referred to the Web version of this article.)

two- and three-dimensional results of AFM are displayed in Fig. 2a. Consistent with the SEM observations (Fig. 1a), Ti-M2# sample showed a smaller nanostructure than Ti-M1# sample. Both the Ra and Rq values of Ti-M1# and Ti-M2# samples were higher than those of Ti sample, especially for Ti-M2# sample. Zeta potential reflects the surface charge of the materials, and the detected result is presented in Fig. 2b. All the samples showed a decreased potential value with an increasing pH of KCl solution. At a pH value of 7.4 (indicated by the purple dotted line), both Ti-M1# and Ti-M2# showed a slightly higher potential value than pure Ti surface, while no significant difference was observed between the two coated samples. Overall, no marked differences in the zeta potentials of the three samples were observed. The water contact angles of various samples are shown in Fig. 2c and exhibited the following trend: Ti>Ti-M1#>Ti-M2#. Because Ti-M1# and Ti-M2# were coated with nano-$Mg(OH)_2$, which is a hydrophilic substance, these two samples were expected to exhibit lower contact angles than Ti sample. According

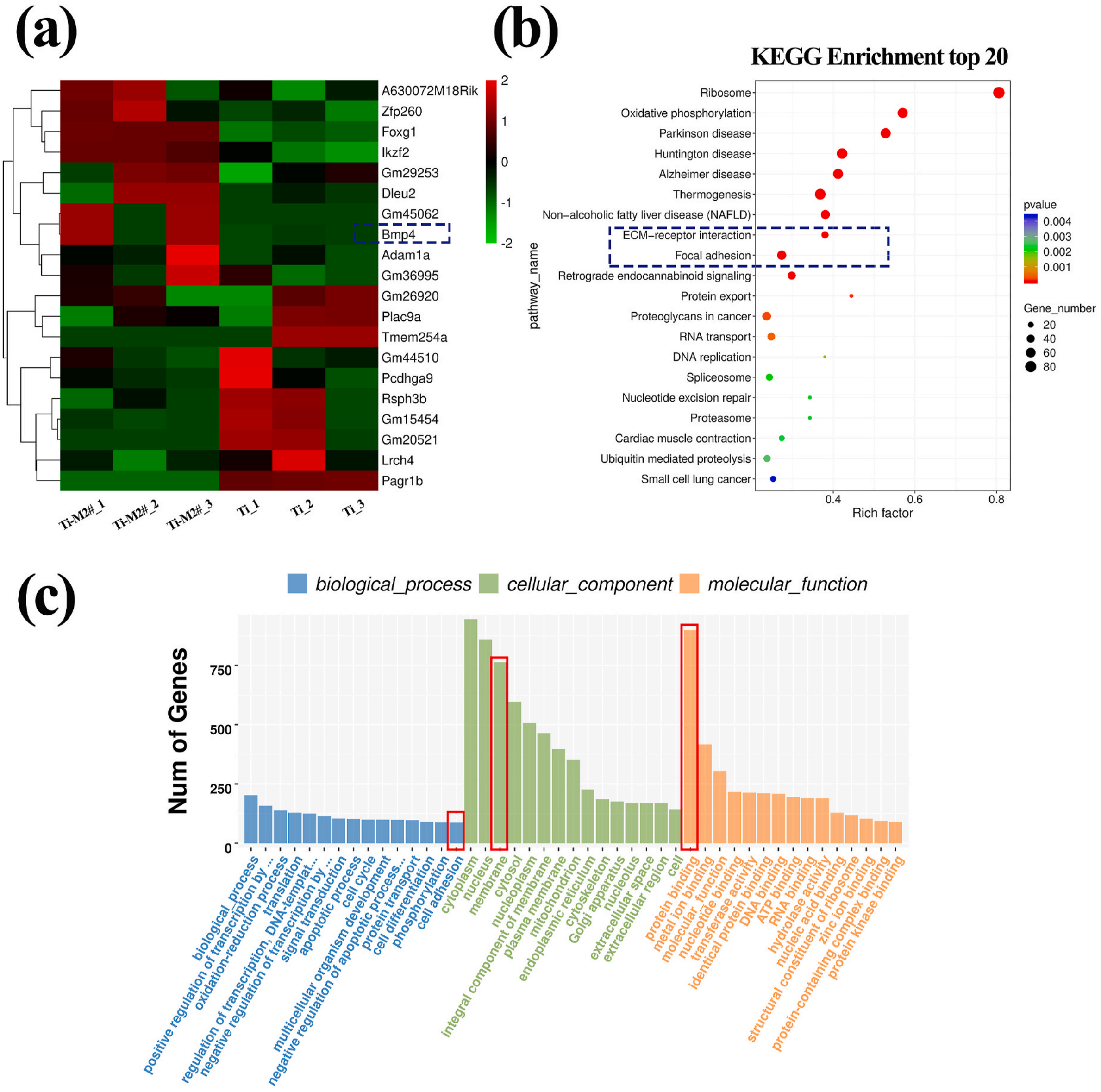

Fig. 8. Heatmap of DEGs of the top 10 upregulated and top 10 downregulated genes of Ti-M2# vs. Ti (a). Analysis of enriched DEGs by GO (b) and KEGG (c) pathways.

to the Cassie wetting model [28], for a hydrophilic surface, increasing roughness results in a decrease in contact angle. Hence, with a higher roughness (Fig. 2a), Ti-M2# sample exhibited a lower contact angle than Ti-M1# sample.

3.2. *In vitro evaluation of nano-Mg(OH)$_2$ coated Ti*

Cell adhesion and spreading is the first step in proliferation and differentiation [29]. In this study, vinculin of murine C3H10T1/2 cells was stained after being cultured for 12 and 24 h. The results are presented in Fig. 3a. After 12 h of culture, the cells on Ti surface showed an elongated shape, while the cells on Ti-M1# and Ti-M2# surfaces showed a relatively polygonal shape, indicating extensive spreading. When the culture time was extended to 24 h, the cells on Ti surfaces exhibited more lamellipodia structures. The cells on Ti-M1# and Ti-M2# samples showed a similar shape to that at 12 h, but with a larger spreading area. These images indicated that cells on Ti-M2# showed the best adhesion and spreading, followed by Ti-M1# and Ti samples. The calculated average coverage ratio of the cells on the surfaces of various samples further proved the conclusion (Fig. 3b). Fig. 3c presents the proliferation rate of the cells cultured on various samples. The proliferation of the cells on each group increased with time, and no significant difference was observed between the groups. Furthermore, the live/dead staining results suggested that nano-Mg(OH)$_2$ film showed no cytocompatibility to the cells (Fig. S2). These results revealed that nano-Mg(OH)$_2$ film is more favorable for the early adhesion and spreading of cells, and does not harm to cell proliferation.

To evaluate the influence of nano-Mg(OH)$_2$ films on the osteogenic behaviors of murine C3H10T1/2 cells, ECM mineralization and ALP activity were evaluated. As shown in Fig. 4a and b, no significant difference was observed for the mineralization of the cells cultured on various samples at day 7. However, at day 14, the mineralization degree of the cells on the sample' surfaces showed following trends: Ti-M2#>Ti-M1#>Ti. The results of the qualitative and quantitative analysis of ALP activity are displayed in Fig. 4c and d, respectively. No significant difference was observed at day 7, which is consistent with the ECM results. At day 14, the cells on Ti-M1# and Ti-M2 samples showed higher ALP activity than on Ti surface, and no significant difference was detected between the two coated groups. Both the evaluations of ECM and ALP activity suggested that cells cultured on nano-Mg(OH)$_2$ coated

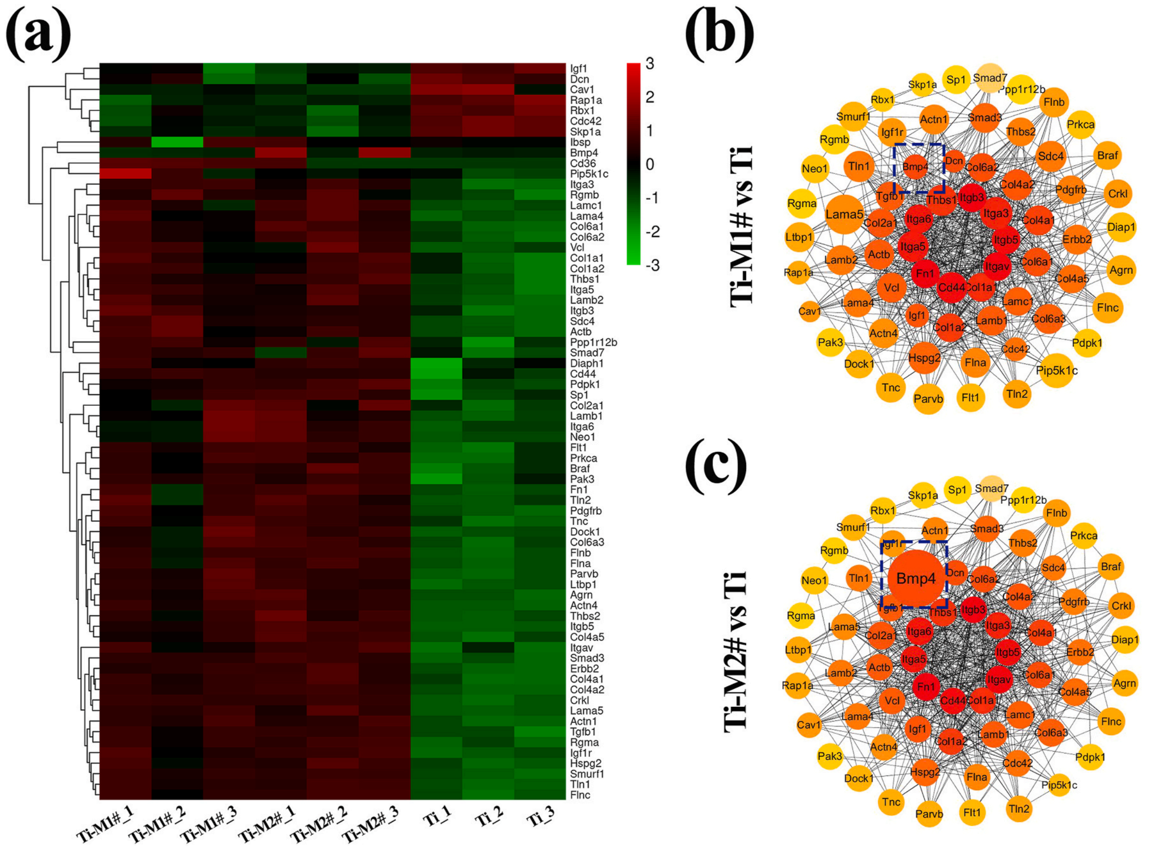

Fig. 9. Heatmaps of DEGs related to ECM-receptor interaction, focal adhesion, and TGF-β pathways (a). PPI networks of Ti-M1# vs Ti (b) and Ti-M2# vs Ti(c).

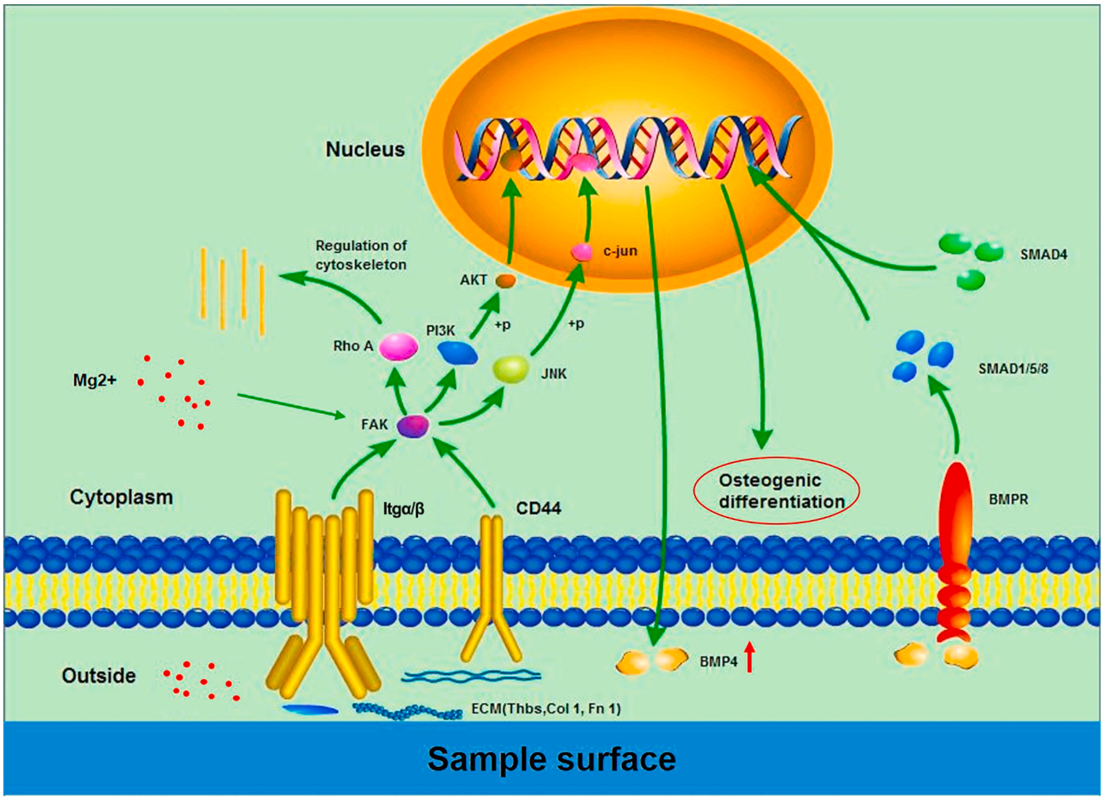

Fig. 10. Potential molecular signaling pathways by which nano-$Mg(OH)_2$ films on Ti surface influence cell behavior.

Ti samples exhibited better osteogenic differentiation. Furthermore, the osteogenesis ability of nano-$Mg(OH)_2$ coated Ti was detected at molecular level. The expression of osteogenesis-related genes in cells cultured on various samples for 7 and 14 days are shown in Fig. 4e and f, respectively. At day 7, although no significant differences were observed for ECM and ALP activity, cells cultured on Ti-M1# and Ti-M2# samples showed significantly higher levels of expression for BMP-2 and OCN genes than on Ti sample. Moreover, a higher level of OPN expression was detected for Ti-M2# group. At day 14, cells on Ti-M1# sample only showed a higher level of expression for BMP-2 gene compared to Ti sample. However, the expression of BMP-2, OCN, and OPN genes remained higher in cells cultured on Ti-M2# sample than those on Ti sample, indicating that osteogenesis was induced more effectively by Ti-M2# sample. In addition, the expression of OCN and OPN proteins detected by western blotting also indicated that cells cultured on Ti-M2# sample showed the best osteogenic differentiation (Fig. S3).

The surface properties of biomaterials determine the fate of adhered cells. As such, a desirable implant should optimize its surface characterization according to the requirements of clinical application. For orthopedic implants, early and fast osteogenesis and osteointegration are the endless pursuit in order to prevent aseptic loosening after implantation [30]. In the present study, nano-$Mg(OH)_2$ films on Ti were designed and fabricated to achieve this aim. The nano-$Mg(OH)_2$ coated samples were covered by nano-sheets which may be the main reason for their better cell adhesion. Meanwhile, the gradual degradation of the $Mg(OH)_2$ coatings would result in the release of Mg ions and the formation of alkaline environments. Mg is a vital component of bone and participates in bone metabolism. More importantly, a study by Zhang et al., proved that Mg ions could promote osteogenic differentiation mediated by calcitonin gene-related peptide (CGRP) [31]. Furthermore, a weakly alkaline microenvironment is also proved effective for the differentiation of osteoblasts [32]. Therefore, nano-$Mg(OH)_2$ samples produce better cell adhesion and osteogenic differentiation results. However, the data on ECM mineralization and the expression of BMP-2, OCN, and OPN genes suggested that the osteogenic induction ability of Ti-M2# sample was superior to that of Ti-M1# sample. Ti-M1# and Ti-M2# samples showed similar Mg ions release ability, contact angles, and zeta potentials, but showed a significantly difference in the size of the nanostructures. Ti-M2# showed a smaller nanostructure. According Yu et al., a smaller nanostructure is more favorable for cell adhesion [33], as observed in the present study. Hence, better adhesion may be responsible for the superior osteogenesis of Ti-M2# sample.

3.3. *In vivo evaluation of nano-$Mg(OH)_2$ coated Ti*

The *in vivo* bone osteointegration of nano-$Mg(OH)_2$ coated Ti was evaluated using a femur implantation model. Fig. 5a shows the 3D-reconstructred micro-CT images of various samples after being implanted for 4 and 8 weeks. After 4 weeks of implantation, only part of Ti implants were surrounded by the newly formed bone, while higher surrounding ratios were observed on Ti-M1# and Ti-M2# implants. When the implantation time was extended to 8 weeks, a layer of more compacted new bone was detected surrounding the Ti-M2# implant, suggesting its better osteointegration. The values of BV/TV and Tb.N calculated according to the micro-CT results are shown in Fig. 5b and c, respectively. Both the BV/TV and Tb.N values of Ti and Ti-M1# groups were in a same level both at weeks 4 and 8. Ti-M2# implant Ti-M2# implant exhibited significantly higher BV/TV value than that of Ti and Ti-M1# both at weeks 4 and week 8. For the values of Tb.N, Ti-M2# showed the higher value than the other two groups at week 4, but no significant difference was detected at week 8 for the three groups.

The new bone formation process surrounding the implants was monitored using sequential fluorescent labeling as shown in Fig. 6a. Small amount of Alizarin red staining were found to be deposited around Ti implants, while more intense and widely Alizarin red staining was observed around Ti-M1# and Ti-M2# implants, especially for Ti-M2# implant. The distribution of Calcein green exhibited a tendency similar to Alizarin red. The MAR and BFR/BS values of various samples were calculated using a combination of images collected at different time points as displayed in Fig. 6b and c, respectively. MAR reflects the ratio of bone mineralization, while BFR/BS represents the activity level of bone formation. Ti and Ti-M1# groups showed no significant difference in MAR and BFR/BS values. Ti-M2# showed both higher MAR and BFR/BS values than the other two groups, indicating it induced the fast and most efficient bone formation process.

Methylene blue acid fuchsin staining was used to investigate the degree of bonding between the newly formed bone and the implants. As shown in Fig. 7a, the new bone formed around Ti-M1# and Ti-M2# implants were thicker and more closely associated with the implant than that surrounding Ti implant at week 4. Eight weeks after their implantation, Ti and Ti-M1# implants showed a similar tendency as that at week 4, while more new bone was found to form and adhere to the Ti-M2# implant, suggesting its superior osteointegration ability. The bone-implant contact ratios of various implants are summarized in Fig. 7b. At week 4, Ti-M1# and Ti-M2# showed significantly higher bone-implant contact ratios than Ti group, especially for Ti-M2# groups. Compared with week 4, the bone-implant ratios of all three groups increased at week 8, but the trend remained as follows: Ti-M2# > Ti-M1# > Ti. The push-out force was used to evaluate the bonding strength between the new bone and the implants, as shown in Fig. 7c. For all three implants, the push-out forces were in the same level at week 4. However, at week 8, the push-out forces of Ti-M1# and Ti-M2# groups were significantly stronger than that of Ti group, especially for the Ti-M2# group. These results suggested that Ti-M2# induced ostoeintegration most efficiently among the three samples.

In general, the *in vivo* results were consistent with the *in vitro* results, which both indicated that nano-$(MgOH)_2$ films are favorable for osteogenesis behaviors, in which Ti-M2# exhibit a better performance than Ti-M1#.

3.4. *Whole genome expression analysis*

To elucidate the molecular mechanism of the enhanced osteogenesis ability of nano-$Mg(OH)_2$ films, whole genome expression analysis was conducted on cells cultured on various surfaces. All Pearson correlation values were higher than 0.92, suggesting a good clustering (Fig. S4a). Ti-M1# and Ti-M2# groups showed few differences in the first principle component, while a slight difference was observed at the second principle component (Fig. S4b). Notably, Ti group exhibited a significant difference with nano-$Mg(OH)_2$ coated groups at both the first and second principles, revealing that the film had an obvious influence on gene expression in the cells. From the volcano plot of DEGs, compared with Ti, the number of significantly upregulated genes in cells cultured on Ti-M1# and Ti-M2# was 36 and 29, respectively, while the downregulated genes weas 147 and 251, respectively (Fig. S5). Furthermore, from the Venn diagram of DEGs (Fig. S6), the DEGs number of Ti-M2# vs Ti and Ti-M1# vs Ti was 280 and 185, respectively. And the co-shared DEGs number was 100.

Fig. 8a shows the heat map of the top 10 upregulated and top 10 downregulated genes of Ti-M2# vs Ti. Among these upregulated genes, BMP-4, a member of the family of bone formation proteins, was closely related to the bone formation process [34]. Thus, all of the signaling pathways that contained BMP4 gene were selected (Table S2). Among these signaling pathways, the TGF-β pathway ($p = 0.36$) mediates signal transduction by transforming growth factors, and thus takes part in a serial of important cell behaviors, such as cell proliferation and differentiation. In this context, we speculated that the TGF-β pathway may be activated by nano-$Mg(OH)_2$ films. The difference between gene expressions was also evaluated using KEGG analysis and Fig. 8b presents the top 20 enrichment pathways. Among these pathways, ECM-receptor interaction pathway plays an important role in maintaining cell structure, and function and focal adhesion pathway determines cell-matrix adhesion and thus influences cell proliferation and differentiation. Therefore, the ECM-receptor and focal adhesion pathways are believed to paly crucial roles in the behavior of cells cultured on nano-$Mg(OH)_2$ films. Furthermore, cell adhesion of biological process, membrane of cellular component, and protein binding for molecular function were observed in the top fifteen GO terms based on the most significant *p*-value (Fig. 8c), further indicated that cell adhesion and cell membrane protein had great influence on cell behavior in this study. From the above analysis, we can conclude that the ECM-receptor interaction, focal adhesion, and TGF-β pathways may be comprised the underlying molecular mechanism by which nano-$Mg(OH)_2$ films influence cell behavior. Hence, we selected all of the DEGs involved in these three pathways for heat-map analysis as shown in Fig. 9a. When cells were cultured on Ti-M1# and Ti-M2# surfaces, most genes were upregulated compared with those cultured on Ti surface. For DEGs related to the ECM-receptor interaction pathway, 30 genes were upregulated and no genes were downregulated (Table S3); For the focal adhesion pathway, 47 genes were upregulated, but only 4 genes were downregulated (Table S4); Lastly, for the TGF-β pathway, 11 genes were upregulated, but only 3 genes were downregulated (Table S5). These DEGs are also presented as protein-protein interactions (PPI) in Fig. 9b and c. The top 10 genes that participated in the interaction are shown in the innermost circle: Itgα5, Itgα6, Thbs1, Itgβ3, Itgα3, Itgβ5, Itgαv, Col1a1, Cd44, Fn1. Among these, the number of genes related to ECM-receptor interaction, focal adhesion, and TGF-β pathways were 10, 8, and 1, respectively. It is worth noting that a major difference between the PPI images of Ti-M1# vs. Ti and Ti-M2# vs. Ti was the expression of the BMP4 gene (indicated by the blue dotted box). Moreover, in the PPI image of Ti-M2# vs. Ti-M1# (Fig. S7), the degree of different expression of BMP4 was the same level as that observed in Ti-M2# vs. Ti. Furthermore, BMP4 was in the top 10 upregulated genes of Ti-M2# vs. Ti (Fig. 8a), but not in that of Ti-M1# vs. Ti (Fig. S8). Hence, compared with Ti-M1# sample, Ti-M2# sample appears to be more effective in activating BMP4 expression.

Previous studies have illustrated that Mg ion is a key factor in modulating the osteogenic differentiation of MSCs. The addition of Mg ions can activate several cell differentiation-related pathways, such as Notch, Rankl, and PI3K/AKT, thereby promoting the transcription of osteogenesis-related genes, including RUNX-2, ALP, and BMP-4 [35–38]. Furthermore, Mg content in bio-ceramic substrate can stimulate the expression of the integrin receptors of BMSCs, affecting the bonding of integrins with sample surface [39,40]. On the other hand, surfaces with micro/nano-structures are more favorable for the identification and deposition of proteins, thus promoting the adhesion and spreading of cells via interactions with integrin [12]. The molecular mechanism of the osteogenic differentiation of nano-$Mg(OH)_2$ coated Ti is depicted in Fig. 10. Based on the results of KEGG pathway enrichment, cell adhesion and integrin were found to be significantly stimulated in Ti-M1# and Ti-M2# groups compared with Ti. Moreover, the key osteogenic differentiation gene, BMP-4, was also found to be significantly promoted. Hence, we speculated that the difference in the Ti-M1# and Ti-M2# groups compared with Ti is mainly be attributed to the participation of Mg ions and the nanostructures, which activate the integrin signaling pathway through extracellular matrix interaction, subsequently activating downstream pathways, such as PI3K-AKT and MAPK. The phosphorylated transcription factors, AKT and c-jun, may be imported into the nucleus, thus promoting the transcription of the BMP-4 gene. In addition, we speculated that the Rho A pathway may participate in the regulation of cytoskeleton, since it is downstream of the integrin pathway. The secreted BMP-4 could further integrate with BMP receptor, thus activating the classic TGF-β signal pathway, mainly smad1/5/8, following the involvement of samd4, together transferred into the nucleus to initiate the osteogenic differentiation process. Interestingly, the cells on Ti-M2# were able to promote BMP-4 expression better than those on Ti-M1#. Taking into account that the amount of Mg ions released from Ti-M1# and Ti-M2# groups were similar, but that Ti-M2# exhibited a narrower microstructure, the superior osteogenesis effect of Ti-M2# could be attributed to the nuances of the micro-morphology of sample surfaces.

4. Conclusions

In this work, nano-$Mg(OH)_2$ films were developed on Ti surface using hydrothermal treatment. $Mg(OH)_2$ films with a nano-sheet-like structure are able to release Mg ions and establish a weakly alkaline microenvironment surrounding the implant. Both the *in vitro* and *in vivo* experiments suggested that nano-$Mg(OH)_2$ coated Ti exhibited a better osteogenesis than Ti alone. Whole genome expression analysis revealed that ECM-receptor interaction, focal adhesion, and TGF-β pathways were activated, resulting in its better osteogenesis. Overall, the use of nano-$Mg(OH)_2$ films is a promising surface modification strategy for the orthopedic application of Ti implants, wherein the study of the molecular mechanisms could be used to guide the design and fabrication of future Ti implants.

CRediT authorship contribution statement

Mengyu Yao: Methodology, Data curation, Formal analysis, Investigation, Writing - original draft. **Shi Cheng:** Methodology, Data curation, Formal analysis, Investigation, Writing - original draft. **Guoqing Zhong:** Investigation, Validation, Methodology. **Jielong Zhou:** Investigation, Validation, Methodology. **Hongwei Shao:** Investigation, Validation, Methodology. **Limin Ma:** Investigation, Validation, Methodology. **Chang Du:** Funding acquisition, Methodology, Project administration, Supervision, Writing - review & editing. **Feng Peng:** Funding acquisition, Methodology, Project administration, Supervision, Writing - review & editing. **Yu Zhang:** Funding acquisition, Methodology, Project administration, Supervision, Writing - review & editing.

Declaration of competing interest

The authors declare no conflict of interest.

Acknowledgements

This work was financially supported by National Key Research and Development Program of China (2017YFB0702604, 2017YFC1105000), National Natural Science Foundation of China (52001076, 31700880), Natural Science Foundation of Guangdong Province, China (2020A1515010827).

Appendix A. Supplementary data

Supplementary data to this article can be found online at https://doi.org/10.1016/j.bioactmat.2021.02.003.

References

[1] M. Geetha, A.K. Singh, R. Asokamani, A.K. Gogia, Ti based biomaterials, the ultimate choice for orthopaedic implants - a review, Prog. Mater. Sci. 54 (2009) 397–425.

[2] A. Barik, N. Chakravorty, Targeted drug delivery from titanium implants: a review of challenges and approaches, in: M. Pokorski (Ed.), Trends in Biomedical Research, 2020, pp. 1–17.

[3] S. Spriano, S. Yamaguchi, F. Baino, S. Ferraris, A critical review of multifunctional titanium surfaces: new frontiers for improving osseointegration and host response, avoiding bacteria contamination, Acta Biomater. 79 (2018) 1–22.

[4] J.J. Cherian, J.J. Jauregui, S. Banerjee, T. Pierce, M.A. Mont, What host factors affect aseptic loosening after THA and TKA? Clin. Orthop. Relat. Res. 473 (2015) 2700–2709.

[5] Y. Wei, Z. Liu, X. Zhu, L. Jiang, W. Shi, Y. Wang, N. Xu, F. Gang, X. Wang, L. Zhao, J. Lin, X. Sun, Dual directions to address the problem of aseptic loosening via electrospun PLGA @ aspirin nanofiber coatings on titanium, Biomaterials 257 (2020), 120237.

[6] J.T. Griffiths, L. Roumeliotis, D.W. Elson, Z.M. Borton, S. Cheung, G.J. Stranks, Long term performance of an uncemented, proximally hydroxyapatite coated,

double tapered, titanium-alloy femoral stem: results from 1465 hips at 10 years minimum follow-up, J. Arthroplasty 36 (2) (2020) 616–622.

[7] L.L. Jia, F.X. Han, H. Wang, C.H. Zhu, Q.P. Guo, J.Y. Li, Z.L. Zhao, Q. Zhang, X. S. Zhu, B. Li, Polydopamine-assisted surface modification for orthopaedic implants, J. Orthopaed. Transl. 17 (2019) 82–95.

[8] Q.G. Wang, P. Zhou, S.F. Liu, S. Attarilar, R.L.W. Ma, Y.S. Zhong, L.Q. Wang, Multi-scale surface treatments of titanium implants for rapid osseointegration: a review, Nanomaterials 10 (6) (2020), 1244.

[9] H.Y. Cheng, H. Hu, G. Li, M. Zhang, K.W. Xiang, Z.H. Zhu, Y. Wan, Calcium titanate micro-sheets scaffold for improved cell viability and osteogenesis, Chem. Eng. J. 389 (2020), 124400.

[10] X.L. Zhu, J. Chen, L. Scheideler, R. Reichl, J. Geis-Gerstorfer, Effects of topography and composition of titanium surface oxides on osteoblast responses, Biomaterials 25 (2004) 4087–4103.

[11] N. Lopez-Valverde, J. Flores-Fraile, J.M. Ramirez, B.M. de Sousa, S. Herrero-Hernandez, A. Lopez-Valverde, Bioactive surfaces vs. Conventional surfaces in titanium dental implants: a comparative systematic review, J. Clin. Med. 9 (7) (2020), 2047.

[12] P. Elter, R. Lange, U. Beck, Atomic force microscopy studies of the influence of convex and concave nanostructures on the adsorption of fibronectin, Colloids Surf. B Biointerfaces 89 (2012) 139–146.

[13] A. Hoppe, N.S. Guldal, A.R. Boccaccini, A review of the biological response to ionic dissolution products from bioactive glasses and glass-ceramics, Biomaterials 32 (2011) 2757–2774.

[14] K.L. Lin, L.G. Xia, H.Y. Li, X.Q. Jiang, H.B. Pan, Y.J. Xu, W.W. Lu, Z.Y. Zhang, J. Chang, Enhanced osteoporotic bone regeneration by strontium-substituted calcium silicate bioactive ceramics, Biomaterials 34 (2013) 10028–10042.

[15] Y.X. Lai, Y. Li, H.J. Cao, J. Long, X.L. Wang, L. Li, C.R. Li, Q.Y. Jia, B. Teng, T. T. Tang, J. Peng, D. Eglin, M. Alini, D.W. Grijpma, G. Richards, L. Qin, Osteogenic magnesium incorporated into PLGA/TCP porous scaffold by 3D printing for repairing challenging bone defect, Biomaterials 197 (2019) 207–219.

[16] M. Harada, N. Udagawa, K. Fukasawa, B.Y. Hiraoka, M. Mogi, Inorganic pyrophosphatase activity OF purified bovine pulp alkaline-phosphatase at physiological PH, J. Dent. Res. 65 (1986) 125–127.

[17] J. Tan, D.H. Wang, H.L. Cao, Y.Q. Qiao, H.Q. Zhu, X.Y. Liu, Effect of local alkaline microenvironment on the behaviors of bacteria and osteogenic cells, ACS Appl. Mater. Interfaces 10 (2018) 42018–42029.

[18] J.H. Li, X.Y. Liu, Y.Q. Qiao, H.Q. Zhu, J.B. Li, T. Cui, C.X. Ding, Enhanced bioactivity and bacteriostasis effect of TiO2 nanofilms with favorable biomimetic architectures on titanium surface, RSC Adv. 3 (2013) 11214–11225.

[19] X.C. Zhao, X.J. Ren, C.Z. Wang, B.X. Huang, J. Ma, B. Ge, Z.F. Jia, Y.C. Li, Enhancement of hydroxyapatite formation on titanium surface by alkali heat treatment combined with induction heating and acid etching, Surf. Coating. Technol. 399 (2020), 126173.

[20] X. Chen, R.F. Zhu, H. Gao, W.L. Xu, G.Y. Xiao, C.Z. Chen, Y.P. Lu, A high bioactive alkali-treated titanium surface induced by induction heat treatment, Surf. Coating. Technol. 385 (2020), 125362.

[21] Q.M. Zhao, G.H. Xu, A.N. Hu, R.S. Xu, H.R.C. Jin, Y.Y. Sun, G.F. Ban, K. Yuan, X. G. Zhou, X. Wang, Z.M. Gui, A Mg/Zn-co-doped composite coating on a titanium surface enhances osteogenic activity through the Wnt/beta-catenin pathway, Appl. Surf. Sci. 515 (2020), 146072.

[22] Q.M. Zhao, X.K. Li, S. Guo, N. Wang, W.W. Liu, L. Shi, Z. Guo, Osteogenic activity of a titanium surface modified with silicon-doped titanium dioxide, Mater. Sci. Eng., C Mater. Biol. Appl. 110 (2020), 110682.

[23] H. Wang, C. Lin, X. Zhang, K. Lin, X. Wang, S.G. Shen, Mussel-inspired polydopamine coating: a general strategy to enhance osteogenic differentiation and osseointegration for diverse implants, ACS Appl. Mater. Interfaces 11 (2019) 7615–7625.

[24] W.E. Samsa, M.K. Mamidi, L.A. Bashur, R. Elliott, A. Miron, Y. Chen, B. Lee, E. M. Greenfield, R. Chan, D. Danielpour, G. Zhou, The crucial p53-dependent oncogenic role of JAB1 in osteosarcoma in vivo, Oncogene 39 (2020) 4581–4591.

[25] A. Gao, Q. Liao, L. Xie, G. Wang, W. Zhang, Y. Wu, P. Li, M. Guan, H. Pan, L. Tong, P.K. Chu, H. Wang, Tuning the surface immunomodulatory functions of polyetheretherketone for enhanced osseointegration, Biomaterials 230 (2020) 119642.

[26] Z. Wang, X. Wang, Y. Tian, J. Pei, J. Zhang, C. Jiang, J. Huang, Z. Pang, Y. Cao, X. Wang, S. An, X. Wang, H. Huang, G. Yuan, Z. Yan, Degradation and osteogenic induction of a SrHPO4-coated Mg-Nd-Zn-Zr alloy intramedullary nail in a rat femoral shaft fracture model, Biomaterials 247 (2020) 119962.

[27] L. Chen, D. Wang, F. Peng, J. Qiu, L. Ouyang, Y. Qjao, X. Liu, Nanostructural surfaces with different elastic moduli regulate the immune response by stretching macrophages, Nano Lett. 19 (2019) 3480–3489.

[28] D.W. Zhang, L.T. Wang, H.C. Qian, X.G. Li, Superhydrophobic surfaces for corrosion protection: a review of recent progresses and future directions, J. Coating Technol. Res. 13 (2016) 11–29.

[29] U. Hersel, C. Dahmen, H. Kessler, RGD modified polymers: biomaterials for stimulated cell adhesion and beyond, Biomaterials 24 (2003) 4385–4415.

[30] C. Kenney, S. Dick, J. Lea, J. Liu, N.A. Ebraheim, A systematic review of the causes of failure of Revision Total Hip Arthroplasty, J. Orthop. 16 (2019) 393–395.

[31] Y. Zhang, J. Xu, Y.C. Ruan, M.K. Yu, M. O'Laughlin, H. Wise, D. Chen, L. Tian, D. Shi, J. Wang, S. Chen, J.Q. Feng, D.H. Chow, X. Xie, L. Zheng, L. Huang, S. Huang, K. Leung, N. Lu, L. Zhao, H. Li, D. Zhao, X. Guo, K. Chan, F. Witte, H. C. Chan, Y. Zheng, L. Qin, Implant-derived magnesium induces local neuronal production of CGRP to improve bone-fracture healing in rats, Nat. Med. 22 (2016) 1160–1169.

[32] J.D. Kaunitz, D.T. Yamaguchi, TNAP, TrAP, ecto-purinergic signaling, and bone remodeling, J. Cell. Biochem. 105 (2008) 655–662.

[33] W.Q. Yu, X.Q. Jiang, F.Q. Zhang, L. Xu, The effect of anatase TiO2 nanotube layers on MC3T3-E1 preosteoblast adhesion, proliferation, and differentiation, J. Biomed. Mater. Res. 94A (2010) 1012–1022.

[34] K. Tsuji, K. Cox, A. Bandyopadhyay, B.D. Harfe, C.J. Tabin, V. Rosen, BMP4 is dispensable for skeletogenesis and fracture-healing in the limb, J. Bone Joint Surg. Am. 90 (2008) 14–18.

[35] M. Zhang, C. Wu, K. Lin, W. Fan, L. Chen, Y. Xiao, J. Chang, Biological responses of human bone marrow mesenchymal stem cells to Sr-M-Si (M = Zn, Mg) silicate bioceramics, J. Biomed. Mater. Res. 100 (2012) 2979–2990.

[36] S. Yoshizawa, A. Brown, A. Barchowsky, C. Sfeir, Magnesium ion stimulation of bone marrow stromal cells enhances osteogenic activity, simulating the effect of magnesium alloy degradation, Acta Biomater. 10 (2014) 2834–2842.

[37] L. Wu, F. Feyerabend, A.F. Schilling, R. Willumeit-Römer, B.J.C. Luthringer, Effects of extracellular magnesium extract on the proliferation and differentiation of human osteoblasts and osteoclasts in coculture, Acta Biomater. 27 (2015) 294–304.

[38] W. Paul, C.P. Sharma, Effect of calcium, zinc and magnesium on the attachment and spreading of osteoblast like cells onto ceramic matrices, J. Mater. Sci. Mater. Med. 18 (2007) 699–703.

[39] H. Zreiqat, C.R. Howlett, A. Zannettino, P. Evans, G. Schulze-Tanzil, C. Knabe, M. Shakibaei, Mechanisms of magnesium-stimulated adhesion of osteoblastic cells to commonly used orthopaedic implants, J. Biomed. Mater. Res. 62 (2002) 175–184.

[40] J. Zhang, X. Ma, D. Lin, H. Shi, Y. Yuan, W. Tang, H. Zhou, H. Guo, J. Qian, C. Liu, Magnesium modification of a calcium phosphate cement alters bone marrow stromal cell behavior via an integrin-mediated mechanism, Biomaterials 53 (2015) 251–264.